Numerical simulation of detonation processes in a variable cross-section chamber

H Y Fan and **F K Lu***
Aerodynamics Research Center, Mechanical and Aerospace Engineering Department, University of Texas at Arlington, Arlington, Texas, USA

The manuscript was received on 3 August 2007 and was accepted after revision for publication on 8 November 2007.

DOI: 10.1243/09544100JAERO272

Abstract: The detonation processes occurring in a combustion chamber with variable cross-sections are numerically simulated for a hydrogen–air reacting flow. The chamber consists of a large diameter tube and two small identical tubes connected on each side through frustums. The channel is closed at the left end and opened at the right. A two-dimensional, time accurate, finite-volume-based method is used to perform the computations. A five-species, two-step global reaction mechanism is used. Two detonation cases are simulated, corresponding to initiation from the closed, left end and the opened, right end. The study showed that area change gave rise to complex wave phenomena. The area change and wave reflections yielded extreme parameters.

Keywords: detonation, shock wave, reactive flow, numerical simulation, variable cross-section chamber

1 INTRODUCTION

Gaseous detonations, with their terrifyingly destructive nature, can nonetheless be exploited for many positive purposes. This subject has received considerable interest for certain applications, such as in propulsion [**1**] and in high-enthalpy ground test facilities [**2**]. The primary advantage of detonation combustion as compared to deflagration is its rapid energy release. This rapid energy release allows the design of pulse detonation engines with high specific power. Although there are many unresolved fundamental issues regarding initiation, transition, and propagation, for example, numerical modelling for obtaining engineering solutions can be sought for the above-mentioned applications. Time-accurate computational fluid dynamics methods can be used to perform cycle analysis and design optimization. An unsteady numerical simulation model was proposed for the purposes described above [**3**]. This two-dimensional, time-accurate, finite-volume-based model has been demonstrated with different example cases to formulate the physical detonation phenomena precisely, including chemical and thermal non-equilibrium.

Most pulse detonation studies, both experimental and numerical, up to date have been performed on simple configurations, namely, a tube of constant cross-section [**1**]. In contrast, Baklanov *et al.* [**4**–**6**] recently performed an experimental study of detonation with variable cross-section chambers. Balkanov *et al.* found the possibility of producing flow parameters more extreme than those behind a stationary detonation wave.

In the current study, the detonation processes occurring in a variable cross-section chamber are simulated for a hydrogen–air reactive flow with the numerical method developed in reference [**3**]. The axisymmetric chamber is formed from a main chamber with a large internal diameter, and two small identically sized tubes that are connected on each side of the main chamber through transitional frustums. The entire configuration is closed at one end and opened at the other end. The reaction mechanism is a five-species, two-step global model. The simulation of detonation processes with different

**Corresponding author: Aerodynamics Research Center, Mechanical and Aerospace Engineering Department, University of Texas at Arlington, Arlington, TX 76019-0018, USA. email: franklu@uta.edu*

initiating locations is carried out. The work is an attempt to obtain a qualitative understanding of detonation phenomena in the variable cross-section chamber through the numerical simulation.

2 FORMULATION OF THE PROBLEM

In the present simulation, the time-dependent two-dimensional Euler equations are used to describe an inviscid, non-heat-conducting, reacting gas flow in which thermal non-equilibrium is modelled with a two-temperature model. For simplicity, these equations are described in the Cartesian coordinate system as

$$\frac{\partial U}{\partial t}+\frac{\partial F}{\partial x}+\frac{\partial G}{\partial y}=\boldsymbol{S} \tag{1}$$

where $\boldsymbol{U}$ is the vector of conserved variables, $\boldsymbol{F}$ and $\boldsymbol{G}$ are the convective flux vectors, and $\boldsymbol{S}$ is the vector of source terms

$$\boldsymbol{U}=\begin{bmatrix}\rho_s\\ \rho u\\ \rho v\\ \rho e_{\mathrm{v}}\\ \rho E\end{bmatrix},\quad \boldsymbol{F}=\begin{bmatrix}\rho_s u\\ \rho u^2+p\\ \rho uv\\ \rho u e_{\mathrm{v}}\\ \rho uE+pu\end{bmatrix}$$
$$\boldsymbol{G}=\begin{bmatrix}\rho_s v\\ \rho uv\\ \rho v^2+p\\ \rho v e_{\mathrm{v}}\\ \rho vE+pv\end{bmatrix},\quad \boldsymbol{S}=\begin{bmatrix}w_s\\ 0\\ 0\\ w_{\mathrm{v}}\\ 0\end{bmatrix} \tag{2}$$

The subscript $s=1, 2, 3, \ldots, N_s$ where N_s is the number of species. The first N_s rows represent species continuity, followed by the two momentum conservation equations for the mixture. The next row describes the rate of change in the vibrational energy, and the final row is the total energy conservation equation. The terms u and v are the velocities in the x and y-directions, respectively, $\rho=\sum_{s=1}^{N_s}\rho_s$ is the mixture density, ρ_s is the density of species s, p is the pressure, e_{v} is the vibrational energy, E is the total energy per unit mass of mixture, w_s is the mass of production rate of species s per unit volume, and w_{v} is the vibrational energy source.

The internal energy based on the two-temperature model is assumed to comprise of an equilibrium portion at the translational temperature T and a non-equilibrium portion at the vibrational temperature T_{v}, and can be defined as

$$e=e_{\mathrm{eq}}(T)+e_{\mathrm{v}}(T_{\mathrm{v}}) \tag{3}$$

where e_{eq} and e_{v} are the equilibrium and non-equilibrium portions of the internal energy. These energy components can be determined with certain thermodynamic relations [**3**].

The source terms for the species mass production rate in the chemical reactions can be written as [**7**]

$$w_s=M_s\sum_{r=1}^{N_{\mathrm{r}}}(\beta_{s,\mathrm{r}}-\alpha_{s,\mathrm{r}})(R_{\mathrm{f,r}}-R_{\mathrm{b,r}}) \tag{4}$$

where M_s is the molecular weight of species s, N_{r} is the number of reactions, $\alpha_{s,\mathrm{r}}$ and $\beta_{s,\mathrm{r}}$ are the stoichiometric coefficients for reactants and products, respectively, in the rth reaction. The forward and backward reaction rates of the rth reaction are $R_{\mathrm{f,r}}$ and $R_{\mathrm{b,r}}$ respectively. These rates can be determined by the Arrhenius law [**3**].

The source term of vibrational energy can be written as

$$w_{\mathrm{v}}=\sum_s Q_{\mathrm{v},s}+\sum_s w_s e_{\mathrm{v},s} \tag{5}$$

The first term on the right-hand side, $Q_{\mathrm{v,s}}$, represents the vibrational energy exchange rate of species s due to the relaxation process with translational energy which can be determined by the Landau–Teller formulation [**3**, **8**–**10**]. The second term, $w_s\ e_{\mathrm{v},s}$, represents the amount of vibrational energy gained or lost due to production or depletion of species s from chemical reactions [**3**].

As mentioned above, the algorithm that is used to solve these equations numerically was described in reference [**3**]. This algorithm is finite-volume based. The advantage of this method is its use of the integral form of the equations, which ensures conservation, and allows the correct treatment of discontinuities. Non-equilibrium flows involving finite-rate chemistry and thermal energy relaxation often can be difficult to solve numerically because of stiffness. The method includes a point implicit treatment of source terms to reduce the inherent stiffness of the system by effectively rescaling all the characteristic times in the fields into the same order of magnitude. Roe's flux-difference split scheme [**11**, **12**] is combined with the Runge–Kutta integration schemes for second-order accuracy in capturing the shock waves in space and time.

In the current study, the hydrogen–air combustion mechanism of five-species (N_2, O_2, H_2, H_2O, and OH) and two-reactions ($H_2+O_2=2OH$ and $2OH+H_2=2H_2O$) proposed by Rogers and Chinitz [**13**] is used. This model was developed to represent hydrogen–air chemical kinetics with as few reaction steps as possible while still giving reasonably accurate global results. In this model,

nitrogen is counted as a collisional partner in the thermodynamic model and relaxation process, but not included in the chemical reaction model since the maximum temperature in the hydrogen–air reaction does not reach the dissociation temperature of nitrogen.

A novel aspect of the numerical method is a 'local ignition averaging model' (LIAM) applied to the global two-step reaction mechanism. As was shown in reference [**3**], for the hydrogen-air reaction process, the mass fraction of some species could change very quickly as soon as the ignition is started. For example, the OH production reaction was instantaneous at its initial stage and went to equilibrium very fast in less than 10^{-12} s. This fact indicates that to ensure that the chemical kinetics are properly followed, the time step in the flow solver should be 10^{-12} s or less. However, it is practically impossible to use this small time step in the flow solver since 10^9 integration steps might be needed to solve a typical detonation wave propagation problem with time scales of 10^{-3} s. The number of steps would result in 10^4 days of CPU time when 1 s of CPU time per computation cycle (which is a proper estimate for this code on a typical front-end workstation) is assumed. This causes a stiffness of the chemical reaction model, which cannot be taken care of by the aforementioned point implicit treatment of source terms. To deal with this stiffness problem, a special treatment is required for the ignition cells. For this purpose LIAM was proposed. The basic idea for this approach comes from the fact that the species mass fractions are changing drastically in a very short period as soon as ignition starts and reaches equilibrium soon afterwards. LIAM separates the cell in which the ignition condition is met and then integrates the chemical kinetics equations alone in that cell. A much smaller time step (e.g. $<10^{-12}$ s) is used in the integration within the interval of the flow solver time step. The average production rate of each species during this time interval is then obtained through dividing the density change of species by the flow solver time step. LIAM turns out to work well with the point implicit scheme to accurately describe chemical kinetics in the flow solver using a typical flow solver time step of 10^{-7} s. Further details on LIAM can be found in references [**3**] and [**14**].

3 CONFIGURATION AND COMPUTATIONAL SET-UP

The chosen numerical method is applied to simulate detonation wave propagation occurring in an axisymmetric chamber. Figure 1 is a schematic of the configuration. The main chamber (segment III) has a 120 mm internal radius and a 200 mm length, while the small tubes (segments I and V) arranged on both sides of segment III have a 20 mm internal radius and a 200 mm length. The total length of the chamber is 800 mm. The chamber's left end is closed and the right end is opened. The chamber is initially filled with a homogeneous stoichiometric hydrogen–air mixture at ambient condition (0.101 325 MPa and 298.15 K). The detonation wave is initiated inside the chamber at two different positions – in the closed end of the detonation chamber, denoted as the left ignition case, and in the open end of the detonation chamber, denoted as the right ignition case. The detonation products expand from the chamber to the surrounding air directly. For both cases, slip conditions are considered on the closed end-wall and the chamber surface. At the flow outlet boundary, that is, at the right-hand boundary, atmospheric conditions are implemented for each case. For both simulation cases, the flow solver time step is 10^{-7} s.

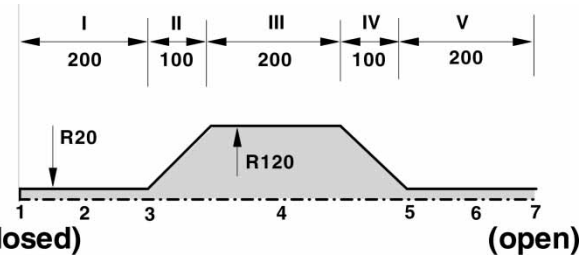

Fig. 1 Schematic of the variable cross-section detonation chamber: the main chamber has a 120 mm internal radius and a 200 mm length; small tubes in both sides of the main chamber have 20 mm internal radius and 200 mm length; 1, 2, . . . ,7, indicate horizontal locations used for displaying data of interest

In the current study, a 'one-shot' detonation process is simulated. The different parts of the computational domain are meshed with structured grids, which are not all identical. A mesh convergence test is performed by trial and error to determine the proper mesh size to ensure the accurate resolution of the physical process, given the current computational power. The associated test result can be found in reference [**15**]. It was shown that when accuracy as well as efficiency is taken into account in choosing the mesh size, the mesh design of 30×400 cells is reasonable and is chosen for the current simulations.

The mesh size as chosen has a horizontal grid spacing of 2 mm. As has been shown in the earlier mesh convergence experiment and in a similar study by

Kim [**14**], with this mesh size, the adopted method can well capture the reaction equilibrium results of a detonation wave. Such a grid scale, however, may be too coarse to resolve the finer spatial detonation feature. For example, if detailed detonation structure such as the cellular structure was intended to be observed, an important characteristic that is needed to be resolved may be the induction layer, a very small zone with no heat release between the shock front and the following reaction zone. For the stoichiometric hydrogen–air mixture in the current study, that induction zone length can be as small as 0.15–0.2 mm [**16**]. This implies that a mesh with 300×4000 cells or more will be necessary if this layer is to be resolved exactly. With the chosen numerical method and the existent computational resource, the simulation on this mesh size will result in an extraordinarily time-consuming effort. However, the present study focuses attention on the large-scale feature of detonation initiation and propagation, the induced wave interactions, and propulsive performance. The selected size is therefore considered to be adequate for the current purpose.

The 'equilibrium hot spot' ignition approach [**14**] is applied to initiate a detonation wave. In this approach, some cells are assigned with a temperature, density (or pressure), and species concentration as an after-burn equilibrium condition. In the current application, this condition is $T = 3000$ K, $\rho = 2.95$ kg/m^3 plus an appropriate five species' concentration. Given the hot spot condition, the success of a detonation initiation then depends on the volume of the hot spot, and there is a critical hot spot volume for a specific detonation problem [**14**]. Here the volume of the hot spot is determined by trial and error. In the left ignition case, five columns of cells adjacent to the closed end wall and ten rows of cells adjacent to the chamber centre-line, in total 5×10 cells, are taken as ignition cells. Similarly, for the right ignition case, a cluster of 5×10 cells adjacent to the exit plane and the centre-line of the detonation chamber are taken as ignition cells.

4 RESULTS AND DISCUSSION

4.1 Overall observation of detonation wave propagation

The propagation of the simulated detonation wave is first presented as the temporal evolution of the computed pressure fields. The associated contours at different times are shown in Fig. 2. The figure clearly shows the propagation of various disturbances, including the detonation waves. Further, the evolution of spatial distributions of pressure and temperature along the centre-line and the chamber wall as the detonation wave develops in the chamber is shown in Fig. 3. From these figures, a general tendency on the intensity of the detonation wave for the two simulated cases can be observed. In each case, the detonation wave, initiated from the ignition spot, very rapidly reaches the Chapman–Jouguet (CJ) state (in the current case, the CJ state is: $p_{CJ} = 1.586$ MPa; $T_{CJ} = 2958$ K; $\rho_{CJ} = 1.54$ kg/m^3 and $D_{CJ} = 1977$ m/s) and becomes established in the small tube in which it is initiated. The wave then exits the small tube and enters the main chamber. The wave intensity decays to below the CJ state. This intensity decrease seems to occur first near the chamber wall. Nevertheless, as the detonation wave moves forward within the main chamber the intensity of the wave recovers. In other words, there appears to be a retransition. For the left ignition case, the retransition returns the wave to the CJ state. For the right ignition case, the wave only recovers slightly and does not completely reach the CJ state. A further abrupt increase in the intensity of the detonation wave appears when its front passes through the converging part (segment IV for left ignition and segment II for right ignition, respectively). In accordance with the retransition phenomenon of the detonation wave in the main chamber, the simulation results indicate that the detonation wave is separated into a shock wave and a flame front. Pressure is used to record the shock wave front and oxygen fraction to record the flame front. The temporal evolution of the detonation wave front is redrawn in Fig. 4. From the figure, it is found that a separation of the detonation wave front appears in both cases: For the left ignition case, the separation occurs only in a very small region just within or near the divergent part, while for the right ignition case, the separation can be found in a large region through the main chamber. The intensity of the propagating detonation wave continues to increase drastically above the CJ state. The detonation wave then enters into the small tube downstream (segment V for left ignition and segment I for right ignition, respectively) and propagates through it, sustaining a higher intensity.

It can be noted that the above detonation propagation situation qualitatively supports the observations of Baklanov *et al.* [**4**], where one of their experimental cases is similar to the current left ignition case in geometric configuration and detonation procedure. Baklanov *et al.*'s measurement results showed that when a well-developed detonation wave in a small tube area enters a large chamber through a divergent section, the wave degenerates and splits into a shock wave and a

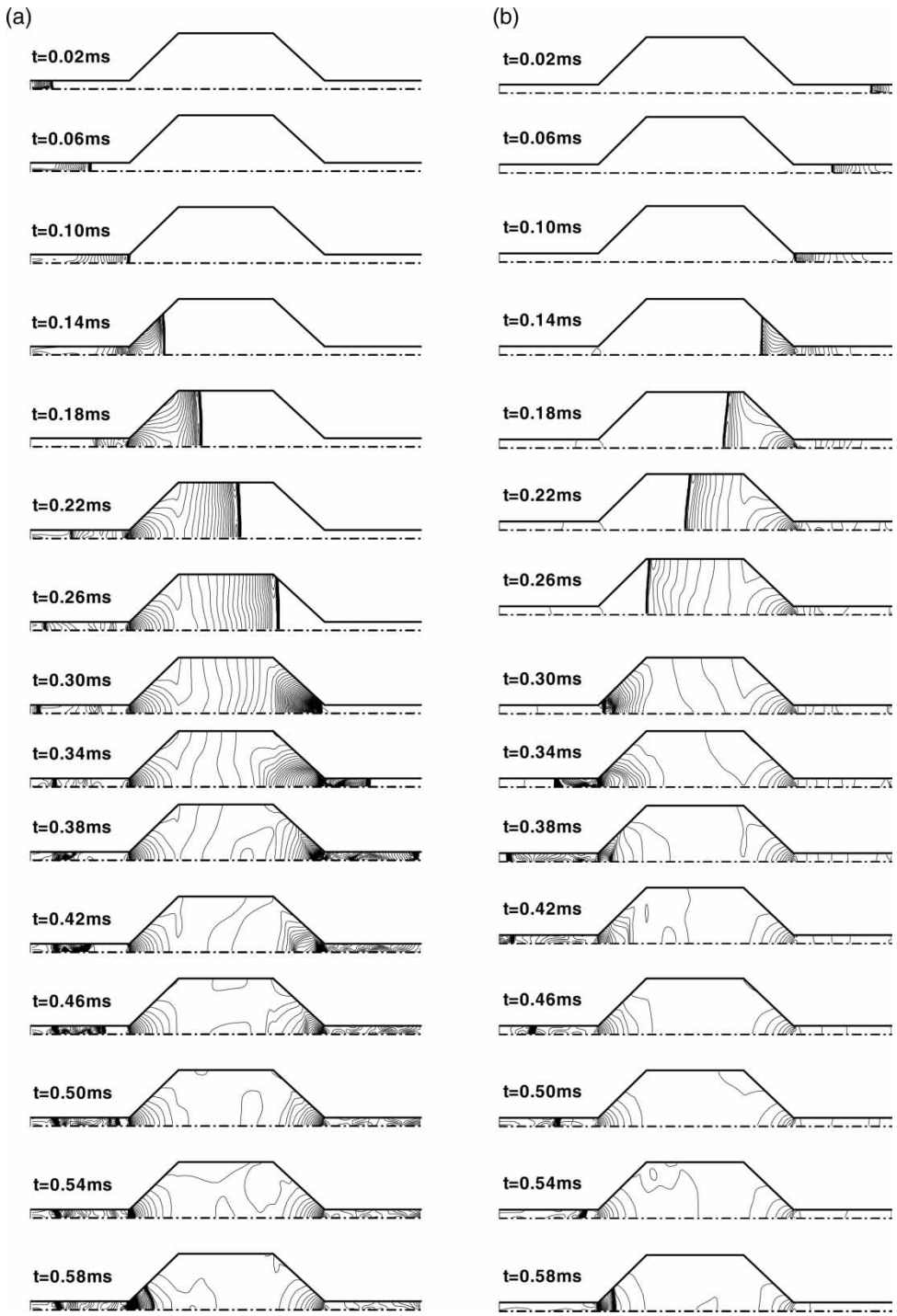

Fig. 2 Pressure contours with data at $t = 0.02 - 0.58$ ms at 0.04 ms interval: (a) left ignition and (b) right ignition

separate flame front. As the shock wave moves forward and further passes through the subsequent convergent part, the detonation wave can be reinitiated by a Mach reflection of the shock wave at the convergent part. Hence, this detonation wave enters the subsequent small tube with a high intensity. In comparing with the results of reference [**4**], the computed detonation wave showed a weaker separation phenomenon. In addition, the simulated cases also do not reproduce the fact that the detonation wave is reinitiated by a Mach reflection of the shock wave on the convergent part. However, the intensity variation of the computed detonation wave in these cases still shows a tendency strongly similar to the experimental observations of reference [**4**].

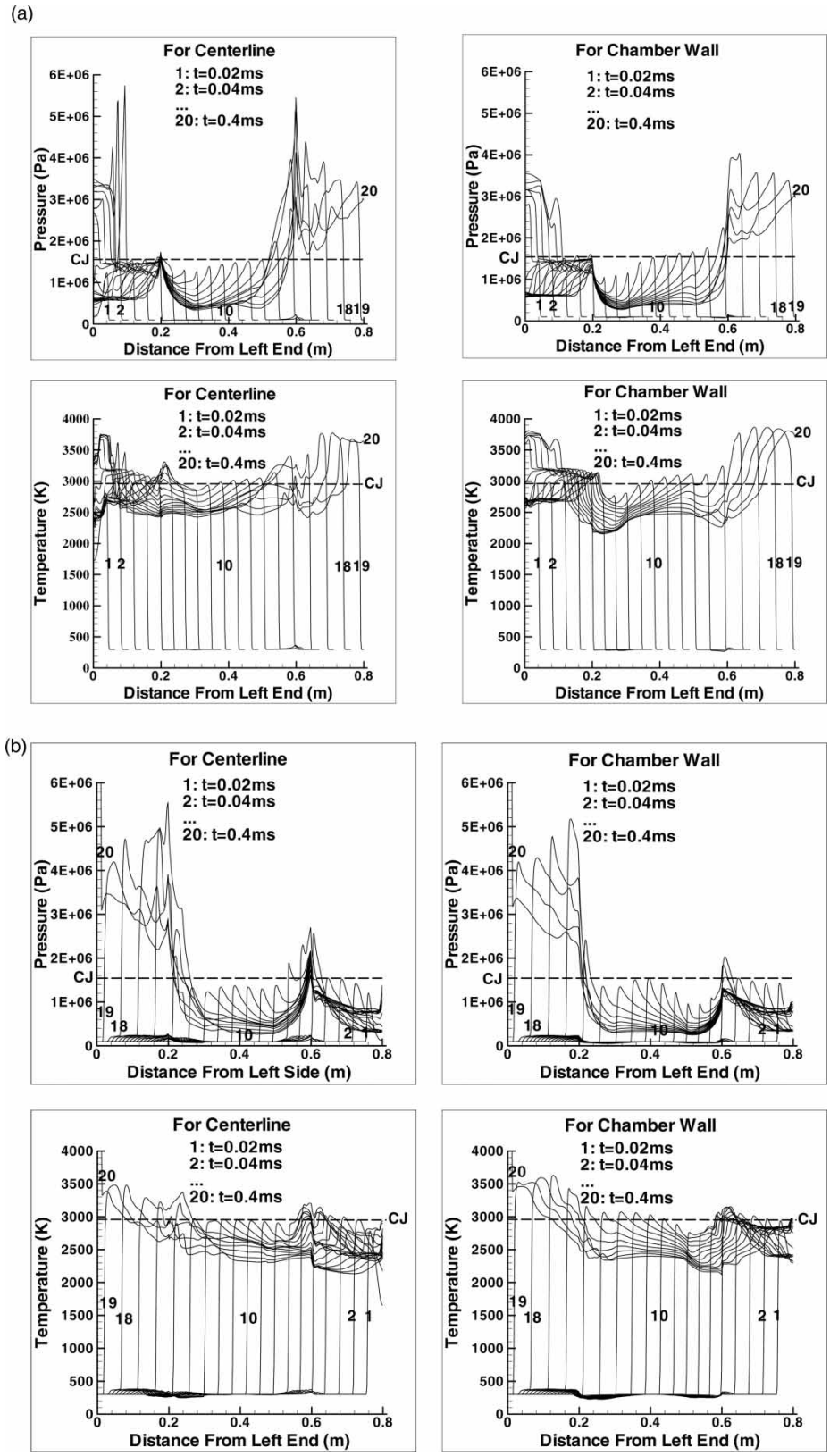

Fig. 3 Evolution of spatial distributions of pressure and temperature along the centre-line and the wall of the detonation chamber, with data at $t = 0.02$–0.60 ms at 0.02 ms interval: (a) left ignition and (b) right ignition

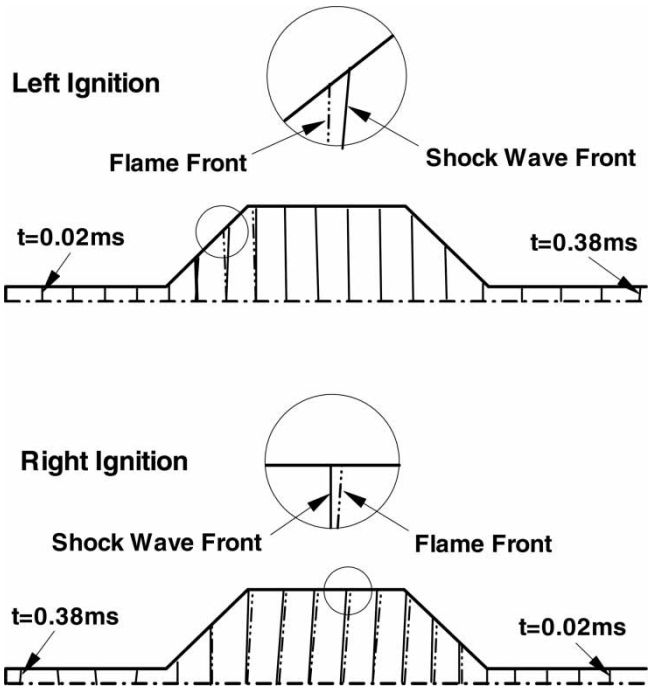

Fig. 4 Evolution of detonation wave front at $t = 0.02$–0.38 ms at 0.02 ms interval. Pressure is used to record the shock wave front (solid line) and oxygen fraction the flame front (dash-dot line)

4.2 Extreme parameters and detonation-induced waves

The simulation results from the two ignition cases show that, as already mentioned above, extreme parameters can be obtained due to area reduction. These parameters can be many times higher than those of the CJ state. This fact can be seen in Figs 2 and 3, and are more clearly presented in Fig. 5. In the latter figure, three parameters, viz., pressure, temperature, and density are used to illustrate the super-CJ state, with peaks appearing in the small tubes at $t = 0.3 - 0.6$ ms. During this time, the detonation wave exits the main chamber and is passing through the corresponding small tubes. Moreover, during this period, for the left ignition case, as the detonation wave strengthens in segment V, a wave reflection occurs in segment I. It can be noted that for the left ignition case, high parameters appear in both of the small tubes (segments I and V) whereas, for the right ignition case, the high values only mainly appear in the small tube area (segment I).

The increase of the intensity of the detonation wave as it enters an area contraction can be attributed to the geometry. In particular, extreme parameters appearing in the small tube area in segment V for the left ignition case is chiefly caused by the convergent part (segment IV), while those in the small tube area in segment I for the right ignition case is partially caused by the convergent part (segment II). (It will be shown later that there are also other reasons yielding the increase of parameters in this area in the latter case.) Baklanov *et al.* [**4**] stated that a convergent part could induce Mach reflection to compress the gas, thereby reigniting the gas to produce a second detonation. However, in each of the simulated cases, the detonation wave is already recovered before it approaches into the convergent part. Hence, the simulations did not reveal a Mach reflection phenomenon and, thus, reignition due to Mach reflection is not observed. Nevertheless, the simulations show an abrupt increase of the intensity of the detonation wave as it enters the convergent part of the chamber. In other words, the area reduction compresses the gas. This implies that the area reduction is an important contributor to the extreme parameters in the subsequent wave propagation in the small tube. It should be mentioned here that the simulation revealed a strong compression of the combustion products behind the detonation wave within the area reduction that is similar to the compression effect of a Mach reflection. However, the simulation is unable to resolve any Mach reflection and a finer grid may be required.

Moreover, the simulation results show that there are various complicated reasons behind the extreme parameters in the small tube areas. Generally, the waves induced during the detonation propagation contribute to the extreme parameters in the small tubes. In the current study, the focus is only on the easily observed waves that are deemed to have a larger effect on the extreme parameter phenomenon.

In the simulation, seven locations, as shown in Fig. 1, are selected along the centre-line of the detonation chamber for further analysis. Interesting flow features, such as shock and detonation fronts, are tracked and displayed in Fig. 6. Wave propagation is displayed in Fig. 7. In these two figures, the detonation wave is represented by the line A1-, A2-, . . . , -A7 for the left ignition case and the line A1′-, A2′-, . . . , -A7′ for the right ignition case. The detonation wave propagates in the detonation chamber with a velocity approximately equal to the CJ ($D_{CJ} = 1977$ m/s) in both ignition cases. These waves are of course the driver of the whole detonation process and the first cause of the extreme parameters in the detonation chambers, especially in the small tubes.

The detailed wave profiles show that other waves are induced by area changes. The left ignition case is considered first. For this case, Fig. 7 shows a wave denoted as A3-B2-B1 that is reflected off the detonation wave near the exit of the small tube in segment I. This wave moves in the tube, in the opposite direction to that of the detonation wave, and reflects

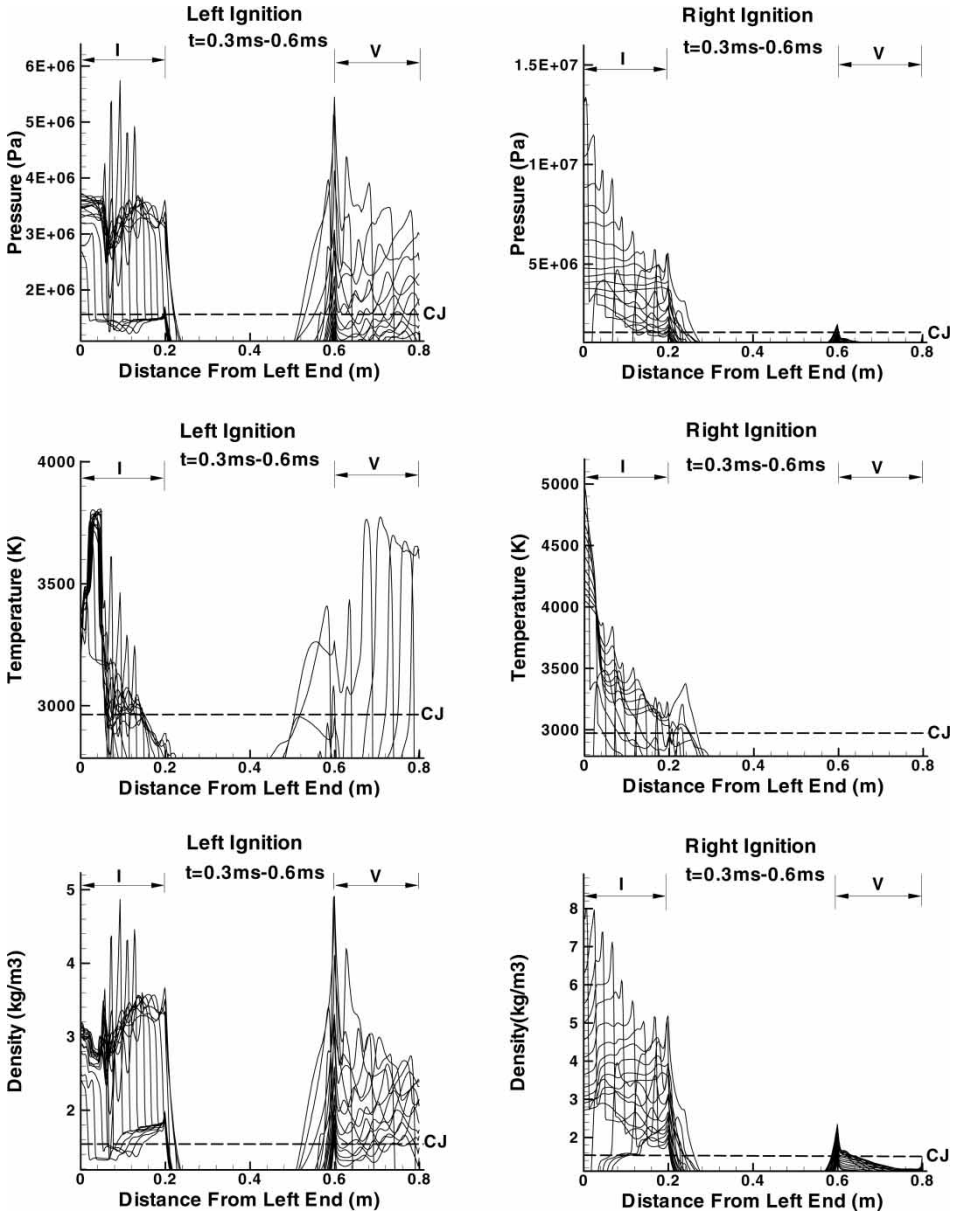

Fig. 5 Peaks of extreme parameters (pressure, temperature, and density) appearing in the small tubes along the chamber centre-line in the two detonation processes for $t = 0.30–0.60$ ms at 0.02 ms interval

off the closed end wall as B1-C2-C3. This latter wave then moves forward toward the main chamber. Therefore, as shown in Fig. 6, within the given computational time period (0–0.6 ms), the reflection wave A3-B2-B1 causes a pressure increase at points 1 and 2 (indicated as B1 and B2, respectively) whereas the secondary reflected wave B1-C2-C3, causes a pressure increase at points 2 and 3 (C2 and C3, respectively).

A more detailed examination of the initiation and propagation of the reflected wave and its reflection at the end wall in segment I for the left ignition case is provided by Fig. 8, which tracks wave propagation in segment I. From this figure and Fig. 7, one can see that the first reflected wave is produced at about $t = 0.12$ ms. This wave propagates back toward the closed end with a low velocity. This wave's propagation speed tends to a constant value of approximately 1450 m/s. Upon reflection from the end wall at about $t = 0.28$ ms, the wave second propagates at approximately 835 m/s.

The right ignition case shows a somewhat simpler wave system than the left ignition case. For this case, there is only an end-wall wave reflection in segment I produced by the incident detonation wave, denoted

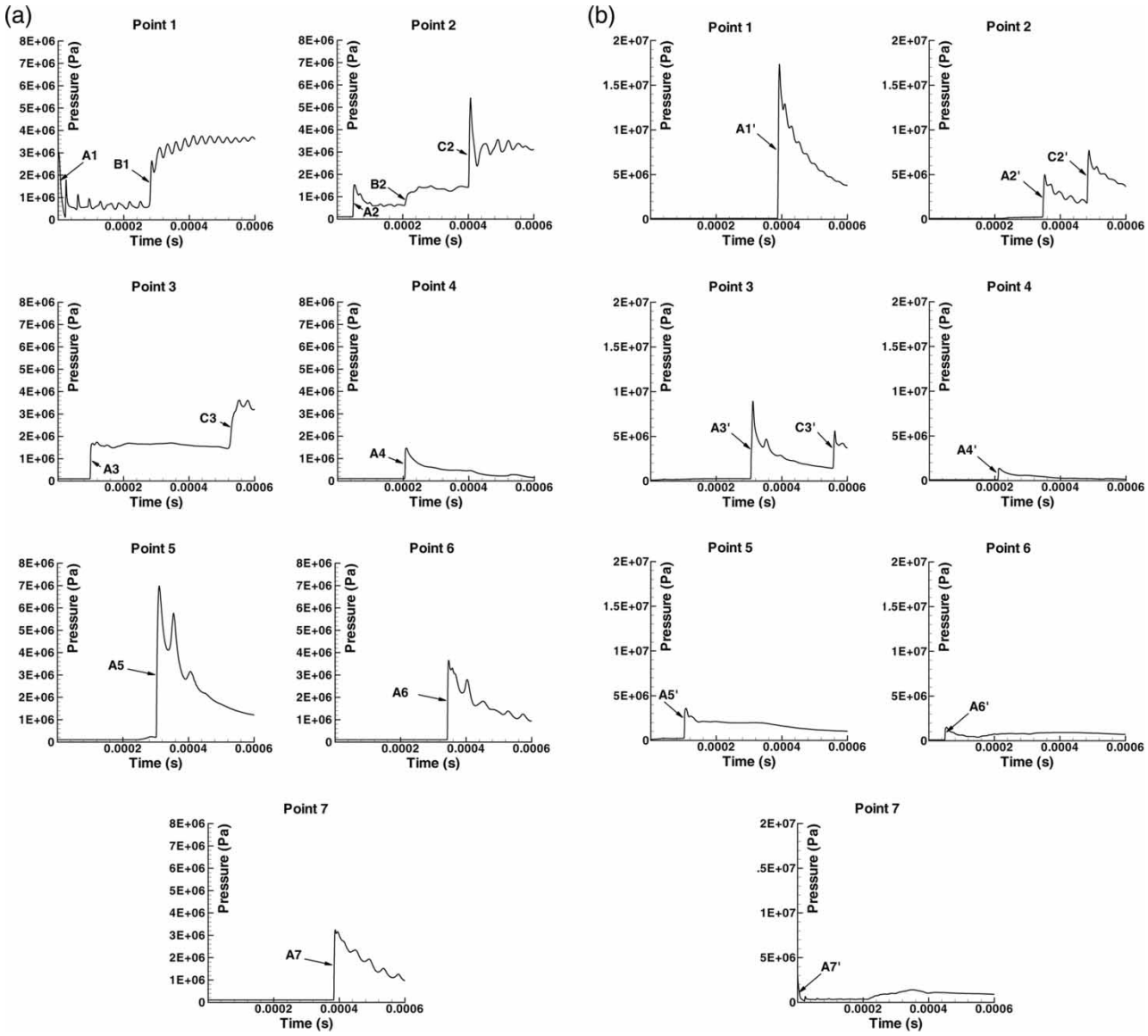

Fig. 6 Temporal evolution of pressure at seven locations (Fig. 1) along the centre-line of the detonation chamber: A1, A2, . . . , A7, and A1′, A2′, . . . , A7′ indicate the pressure increases caused by the detonation wave in the left ignition and right ignition cases, respectively; B1 and B2 indicate the pressure increases caused by a reflected wave, and C2, C3 by a secondary reflected wave, in the left ignition case; C2′ and C3′ indicate the pressure increases caused by a reflected wave in the right ignition case: (a) left ignition and (b) right ignition

as A1′-C2′-C3′ in Fig. 7. In Fig. 6, it can be seen that this reflected wave causes an abrupt pressure increase at points 2 and 3 (C2′ and C3′, respectively) within the computational time period. As for the left ignition case, a more detailed examination of this reflected wave can be made using Fig. 9. From the figure, it is noted that the reflected wave is produced at about $t = 0.39$ ms and propagates towards the main chamber at approximately 1450 m/s.

As can be expected, a detonation process in a variable cross-section chamber should be more complex than that in a simple constant cross-section tube. There appears to be numerous wave disturbances, more than those discussed above, that results in serious non-uniformities and irregular fluctuations. To discuss each of these waves is impossible and beyond the initial aims of this article. Here emphasize is only on phenomena that are most noticeable to highlight the complexity of the wave processes. For example, if the results shown in Fig. 8 are received, during $t = 0.22–0.38$ ms, there is a low-pressure region behind the above-mentioned reflected wave.

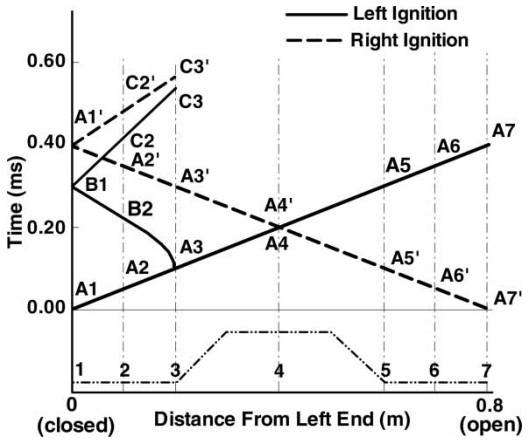

Fig. 7 Wave diagram for the two simulated cases: A1-A2-A3-A4-A5-A6-A7 and A1′-A2′-A3′-A4′-A5′-A6′-A7′ indicate the detonation wave in the left ignition and right ignition cases, respectively; A3-B2-B1 and B1-C2-C3 indicate a reflected wave and a secondary reflected wave in segment I in the left ignition case; A1′-C2′-C3′ indicate a reflection wave in segment I in the right ignition case

The evolution of this region is more clearly seen in the larger images in Fig. 10. This low-pressure region initiates at the small tube (segment I), exits at $t = 0.22$ ms and can be qualitatively explained by one-dimensional wave dynamics. This expansion region moves relatively slowly inside the small tube (with a velocity of approximately 835 m/s) and collides with the second reflected wave (B1-C2-C3 in Fig. 7) at $t = 0.38$ ms. This collision shrinks and annihilates the expansion region, leaving an acoustic wave. Finally, from the analysis, the main contributors to the extreme parameters in the small tube segments for the two detonation processes are summarized in Table 1.

4.3 Propulsion performance

The complex wave systems propagating in the variable cross-section chamber also has an effect on thrust generation, if such a chamber is configured for propulsion, as in a pulse detonation engine. For a generic detonation tube, the thrust produced by a detonation process can be calculated by the classical formula

$$F(t) = \int_0^S \left[(p(t) - p_a) + \rho(t)u^2(t) \right] \mathrm{d}S \tag{6}$$

where p_a is the ambient pressure, and $p(t)$, $\rho(t)$, and $u(t)$ are the instantaneous pressure, density, and horizontal velocity acting on the thrust wall. In equation (6), the integration area S is the area of the walls that the thrust acts on. In the current cases, thrust

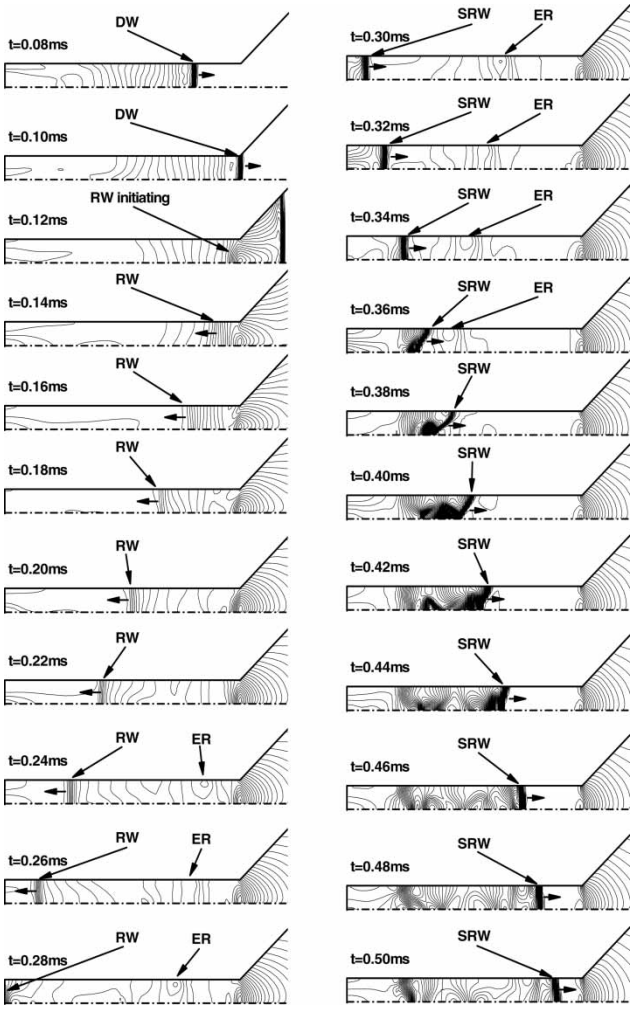

Fig. 8 Production and propagation of the reflected wave (RW) and its secondary reflection (SRW) in segment I for left ignition case. Pressure contours shown at $t = 0.08 - 0.50$ ms at 0.02 ms interval: the reflected wave appears at about $t = 0.12$ ms, and reflects by the closed end at about $t = 0.28$ ms. Note an expansion region (ER) exposes in this figure that moves after the reflected wave and then collides with the secondary reflected wave. DW indicates detonation wave

production occurs on three portions of the tube, as shown in Fig. 11. Besides the portion yielded on the closed end-wall, F_1, thrust is also produced on both of the frustums, namely forces F_2 and F_3. Each thrust portion in the cases can be calculated with the above formula on the associated integration areas.

Impulse is another parameter used to describe the performance of a propulsion system. The impulse is obtained by integrating the thrust from zero to t as

$$I(t) = \int_0^t F(t)\,\mathrm{d}t \tag{7}$$

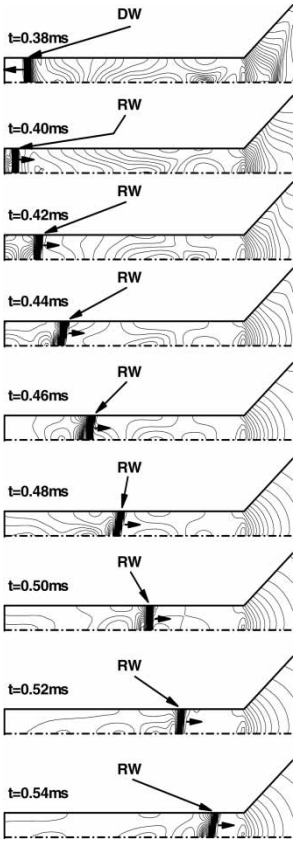

Fig. 9 Production and propagation of a reflected wave (RW) in segment I for right ignition case. Pressure contours shown at $t = 0.38$–0.54 ms at 0.02 ms interval: the reflected wave is initiated at about $t = 0.39$ ms. DW indicates detonation wave

The specific impulse then can be calculated from the relation

$$I_{\mathrm{sp}}(t) = \frac{I(t)}{(\rho_0 V g)} \tag{8}$$

where ρ_0 is the initial density of the reactant gas mixture in the detonation chamber, V is the volume of the chamber, and g is the Earth's sea-level gravitational acceleration. An alternative performance parameter, the fuel-based specific impulse, is also of interest and can be defined as

$$I_{\mathrm{sp,f}}(t) = \frac{I(t)}{(\rho_f V g)} \tag{9}$$

where ρ_{f} is the initial density of the gaseous fuel (hydrogen).

The computations for propulsion parameters are performed with a longer period ($t = 0$–2.5 ms) to allow the detonation processes to sufficiently exhaust to ambient conditions. The thrusts for each of the detonation cases are shown in Fig. 12.

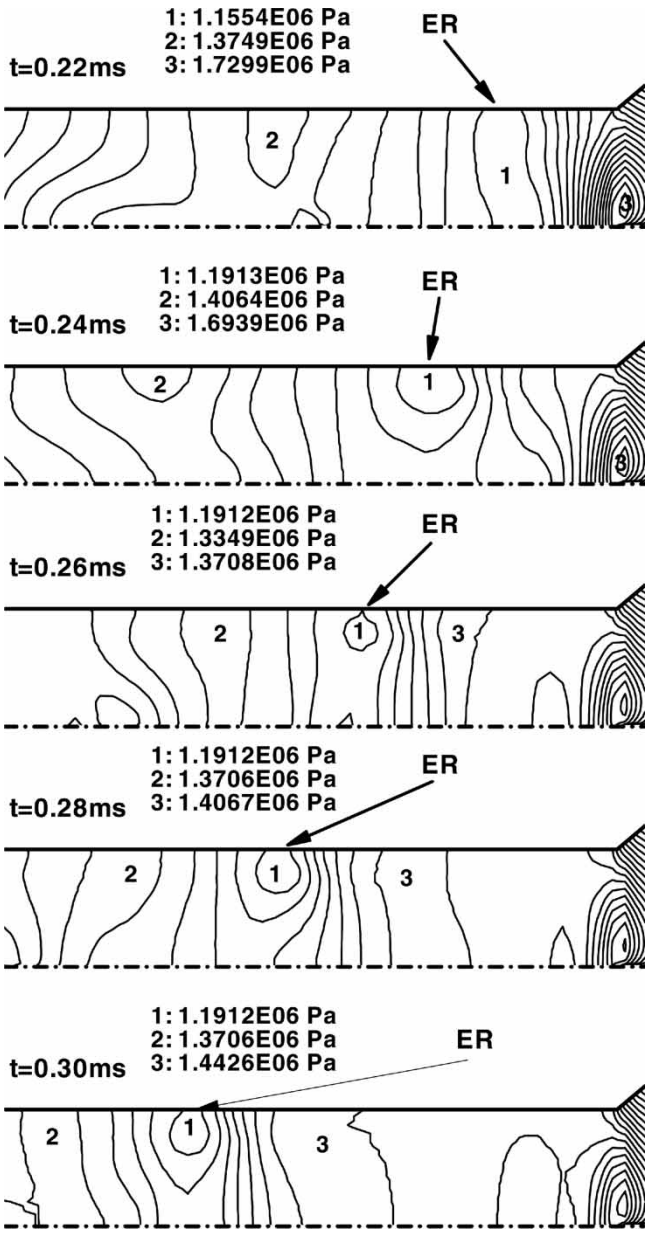

Fig. 10 Production of an expansion region (ER) in the small tube area in the left ignition case: the same phenomenon can also be seen in Figs 2 and 8

Table 1 Summary of the main contributors to extreme parameters in the small tube segments

	In segment I	In segment II
Left ignition	Reflected wave second reflected wave	Tube convergence
Right ignition	Tube convergence reflected wave	

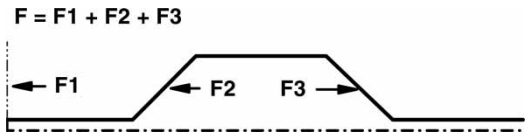

Fig. 11 Three portions of the thrust for detonation processes in the chosen variable cross-section chamber

For each case, the first subfigure in Figs 12(a) and (b) shows the total thrust together with the three portions. The results show that the detonation processes produce complex thrust histories which may be further understood through observing the behaviours of the three thrust portions. The force F_1 yielded on the closed end-wall, for both detonation cases, is produced by the extreme parameters appearing near the end-wall. The left ignition case has relatively constant force F_1 within $t = 0–0.28$ ms since the reflected wave A3-B2-B1 stated in section 4.2 has not yet reached the closed end wall. Thereafter the reflected wave comes and starts to impact the wall, resulting in an abrupt and severe increase in the force level. The higher force level remains for a certain moment and then

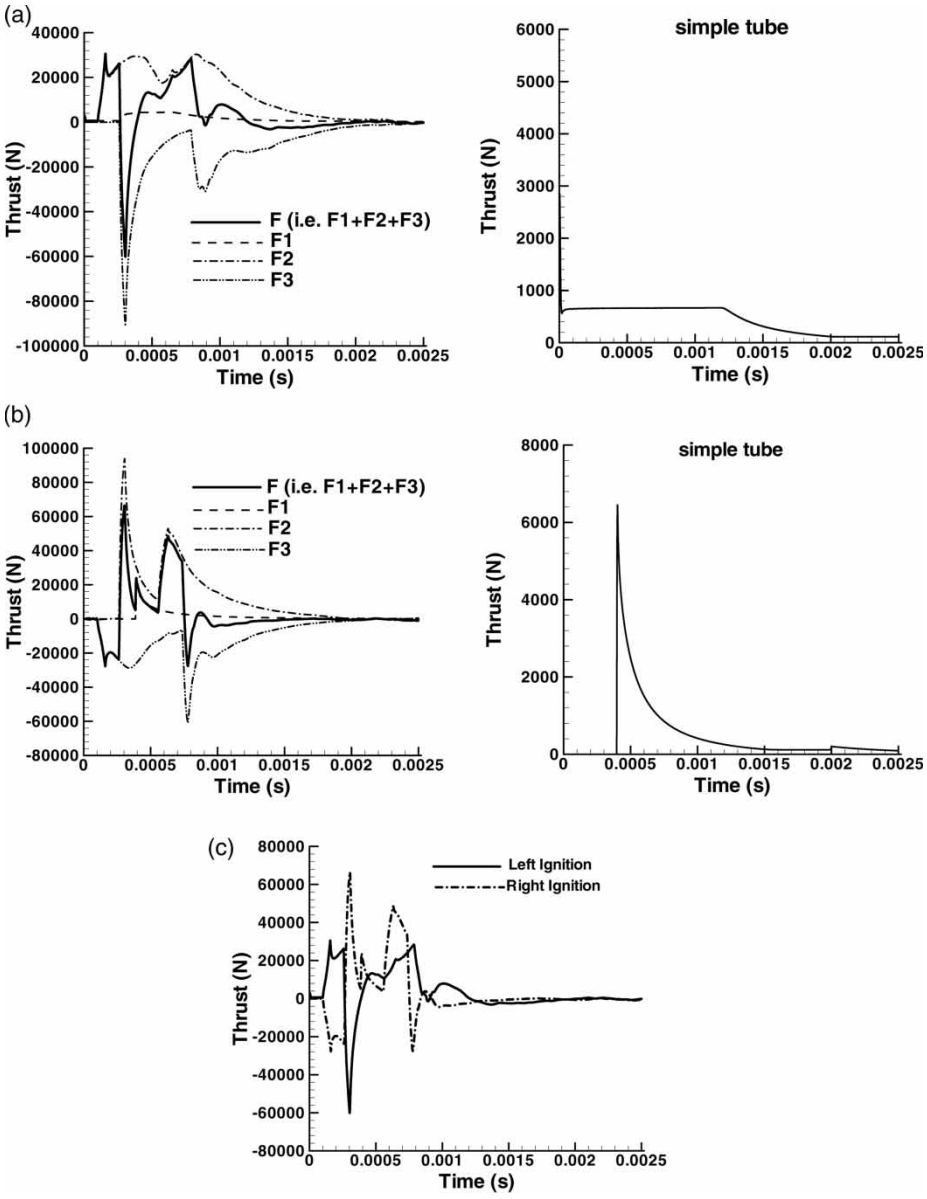

Fig. 12 Thrust obtained from simulation of detonation waves in variable cross-section chamber in comparison with a simple (constant cross-section) tube. The simple detonation tube has 20 mm internal radius and 800 mm total length: (a) thrust in the left ignition case, (b) thrust in the right ignition case, and (c) thrust comparison for both cases

decays gradually to zero. In the right ignition case, a large peak in the force F_1 occurs about 0.4 ms after ignition when the detonation wave reaches the end-wall. The thrust then rapidly decreases to zero.

In both cases, the evolutions of the other two forces F_2 and F_3 are much more complicated. These two forces are first affected by the detonation waves moving through the corresponding frustums. Consequently, the first abrupt increases or decreases on the forces F_2 and F_3, respectively, are yielded by detonation waves. This study shows that reflections off the end-wall have important influences on these two forces. In particular, the left ignition case produces the secondary reflected wave B1-C2-C3 that moves through the small tube area (segment I) and may further move forward to the open end. When the wave pass the segment II, it causes the force F_2 to increase at about $t = 0.6$ ms, and the force F_3 to decrease from about $t = 0.8$ ms. The right ignition case has the reflected wave A1′-C2′-C3′ that also moves through the small tube area (segment I) and may further move forward the open end. When the wave passes segment II, it causes the thrust portion F_2 to increase at about $t = 0.55$ ms, and the thrust portion F_3 to have a decrease at about $t = 0.7$ ms. In both cases, wave propagation through the divergent frustum causes an abrupt decrease in the thrust acting on that frustum (F_2 in left ignition case) or increase (F_3 in right ignition case) followed by a gradual recovery. Finally, Fig. 12(c) summarizes the thrusts produced by the two cases. The average thrusts for the cases are also calculated by

$$\bar{F} = \frac{\int_0^{t_{\max}} F(t)\mathrm{d}t}{t_{\max}} \tag{10}$$

(where $t_{\max} = 2.5$ ms). The results show that the left ignition case has an average thrust (3038 N) that is larger than that of the right ignition case (2671 N).

The defined impulses for each of the detonation cases are shown in Fig. 13. The left ignition and right ignition cases show clearly different behaviours initially. Later, the general trends are similar, with the former case performing a little better that the latter.

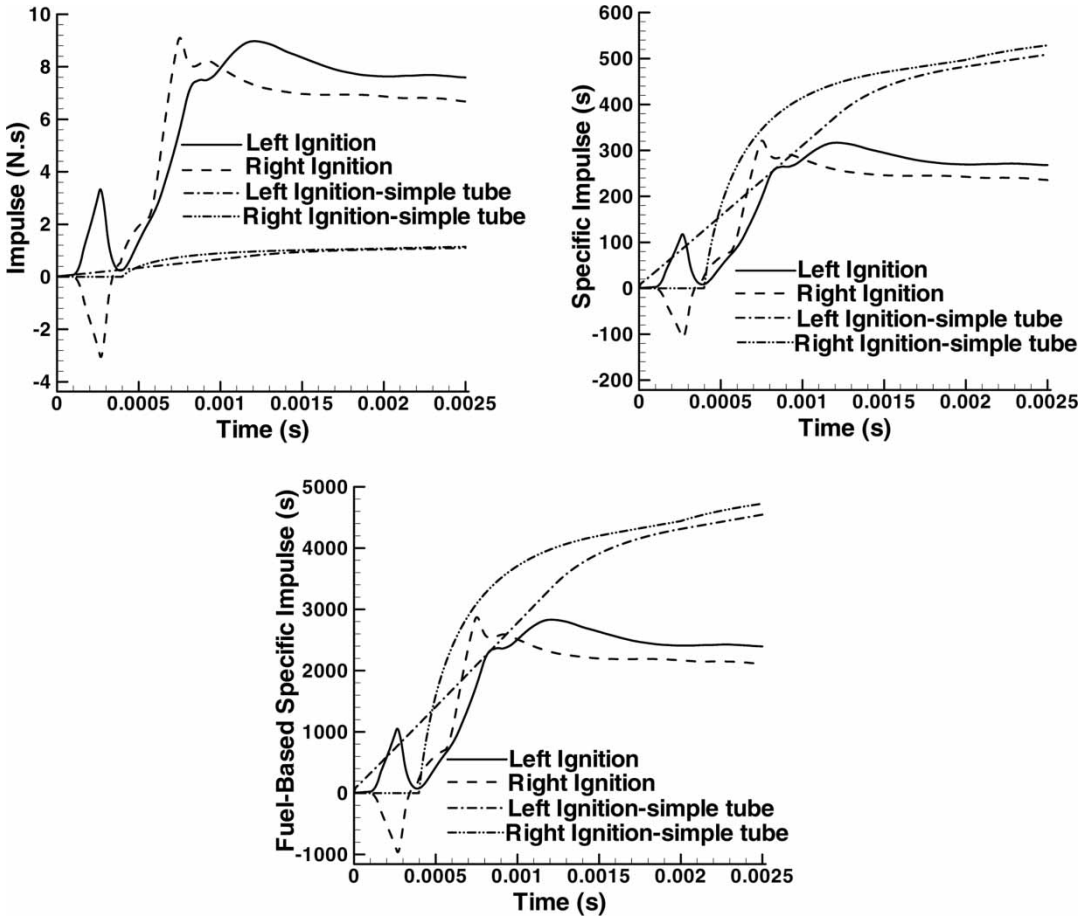

Fig. 13 Impulses obtained from simulation of detonation waves in variable cross-section chamber in comparison with a simple tube

A comparison was also made between these two cases against detonation wave propagation in a constant section tube, again with the left end closed and for the two cases of left and right ignition. The simple tube has the same internal radius (20 mm) as the small tube in the previous cases. Initial conditions remain the same. The thrust and impulse parameters of the detonation processes for the simple-tube case are also shown in Figs 12 and 13. The comparison shows the expected result that the variable cross-section chamber yields much higher thrust and thus higher impulse parameters. However, the specific impulses for the variable cross-section chambers are lower due to the larger quantity of reactants for these two cases compared to the straight tube cases.

5 CONCLUDING REMARKS

A numerical simulation was performed on two-dimensional hydrogen–air detonations occurring in an axis-symmetric variable cross-section combustion chamber. The computational approach used in the simulation is a time-accurate and finite-volume-based method. A five-species and two-step reaction mechanism is adopted to model the thermochemistry of the detonation processes. Two detonation cases, namely, left and right ignition, defined with different initiating locations for the detonations, were studied. The simulation results rebuilt some phenomena that were experimentally observed in reference [**4**]. In both simulated detonation processes, extreme parameters within the small tubes were observed. It was thought that reflected waves appearing in the detonations and area reduction were responsible for the extreme parameters. The following facts in the detonation wave were found: in the left ignition case, extreme parameters appeared in both small tube segments. In segment V, the extreme parameters were produced by area reduction while in segment I they were produced by multiple wave reflections. In the right ignition case, extreme parameters appeared in the small tubes due to a combination of area reduction and wave reflection. Finally, though it is hard to make a comparison of the propulsion performance to decide which case is better than another, the results still showed that the left ignition case performed better a little than its partner in the impulse viewpoint.

REFERENCES

1 **Kailasanath, K.** Recent developments in the research on pulse detonation engines. *AIAA J.*, 2003, **41**(2), 145–159.
2 **Lu, F. K., Wilson, D. R., Bakos, R.,** and **Erdos, J. I.** Recent advances in detonation techniques for high-enthalpy facilities. *AIAA J.*, 2000, **38**(9), 1676–1684.
3 **Kim, H., Lu, F. K., Anderson, D. A.,** and **Wilson, D. R.** Numerical simulation of detonation process in a tube. *Comput. Fluid Dyn. J.*, 2003, **12**(2), 227–241.
4 **Baklanov, D. I., Gvozdeva, L. G.,** and **Scherbak, N. B.** Formation of high-speed gas flow at combustion in the regime of multi-step detonation. In *Gaseous and heterogeneous detonations, science to application* (Eds G. Roy, S. Frolov, K. Kailasanath, and N. Smirnov), 1999, pp. 141–152 (ENAS Publishers, Moscow).
5 **Baklanov, D. I.** and **Gvozdeva, L. G.** Nonstationary processes during propagation of detonation waves in channels of variable cross section. *High Temp.*, 1995, **33**(6), 955–958.
6 **Baklanov, D. I.** and **Gvozdeva, L. G.** The effect of additional ignition on the stability of emergence of the mode of double nonstationary discontinuity in combustors. *High Temp.*, 1996, **34**(2), 294–297.
7 **Gnoffo, P. A., Gupta, R. N.,** and **Shinn, J. L.** Conservation equations and physical models for hypersonic air flows in thermal and chemical nonequilibrium. NASA TP-2867, 1989.
8 **Candler, G. V.** *The computation of weakly ionized hypersonic flows in thermo-chemical nonequilibrium.* PhD Thesis, Stanford University, 1988.
9 **Millikan, R. C.** and **White, D. R.** Systematics of vibrational relaxation. *J. Chem. Phys.*, 1963, **39**(12), 3209–3213.
10 **Vincenti, W. G.** and **Kruger, C. H.** *Introduction to physical gas dynamics,* 1977 (Krieger, Malabar, Florida).
11 **Roe, P. L.** Approximate Riemann solvers, parameter vectors, and difference schemes. *J. Comput. Phys.*, 1981, **43**(2), 357–372.
12 **Grossman, B.** and **Cinnella, P.** Flux-split algorithms for flows with nonequilibrium chemistry and vibrational relaxation. *J. Comput. Phys.*, 1990, **88**(1), 131–168.
13 **Rogers, R. C.** and **Chinitz, W.** Using a global hydrogen–air combustion model in turbulent reacting flow calculations. *AIAA J.*, 1983, **21**(4), 586–592.
14 **Kim, H.** *Numerical simulation of transient combustion process in pulse detonation wave engines.* PhD Thesis, The University of Texas at Arlington, 2000.
15 **Fan, H. Y.** and **Lu, F. K.** Comparison of detonation processes in a variable cross section chamber and a simple tube. *J. Propuls. Power*, 2005, **21**(1), 65–75.
16 **Lu, T., Law, C. K.,** and **Ju, Y.** Some aspects of chemical kinetics in Chapman–Jouguet detonation: induction length analysis. *J. Propuls. Power*, 2003, **19**(5), 901–907.